remote sensing

MDPI

Article

Comparison and Synthesis of Precipitation Data from CloudSat CPR and GPM KaPR

Yanzhi Liang [1], Leilei Kou [1,2,*], Anfan Huang [1], Haiyang Gao [1,2], Zhengjian Lin [3], Yanqing Xie [4] and Liguo Zhang [4]

[1] School of Atmospheric Physics, Nanjing University of Information Science and Technology, Nanjing 210044, China; 20211205006@nuist.edu.cn (Y.L.); gaohy@nuist.edu.cn (H.G.)
[2] Collaborative Innovation Center on Forecast and Evaluation of Meteorological Disasters, Key Laboratory for Aerosol-Cloud-Precipitation of China Meteorological Administration, Nanjing University of Information Science and Technology, Nanjing 210044, China
[3] Hainan Province Meteorological Detection Center, Haikou 570203, China
[4] Shanghai Institute of Satellite Engineering, Shanghai 201109, China
* Correspondence: 002358@nuist.edu.cn

Abstract: Employing different bands of radar to detect precipitation information in identical regions enables the acquisition of a more comprehensive precipitation cloud structure, thereby refining the continuity and completeness of precipitation measurements. This study first compared the coincident data from CloudSat W-band cloud profiling radar (CPR) and Global Precipitation Measurement Mission (GPM) Ka-band precipitation radar (KaPR) from 2014 to 2017, and then a synthesis of the radar reflectivity from CPR and KaPR was attempted to obtain a complete cloud and precipitation structure. The findings of the reflectivity comparisons indicated that the echo-top height identified by CPR is on average 3.6 to 4.2 km higher than that from KaPR, due to the higher sensitivity. Because of strong attenuation of CPR by liquid-phase particles, the reflectivity below the height of the melting layer usually shows an opposite gradient to KaPR with decreasing altitude. The difference in the near-surface rain rates of CPR and KaPR was found to be related to reflectivity gradients in the vertical direction, and the larger the reflectivity gradients, the greater the differences in near-surface rain rates. For better representing the complete vertical structure of precipitation clouds and improving the consistency of the reflectivity and precipitation rate, the radar reflectivity was weighted, synthesized from CPR and KaPR based on the gradient difference of the reflectivity from the two radars. We presented the synthesis results for a stratiform cloud and a deep convective case, and Spearman's rank correlation coefficient (r_s) between the GPM combined radiometer precipitation rate and the radar reflectivity was utilized to analyze the performance of the synthesis. The consistency between synthesized reflectivity and precipitation rate in the non-liquid phase was improved compared with KaPR, and the r_s of the ice and mixed phases was increased by about 12% and 10%, respectively.

Keywords: CloudSat cloud profiling radar (CPR); Global Precipitation Measurement Mission (GPM) Ka-band precipitation radar (KaPR); precipitation data; comparison; synthesis

Citation: Liang, Y.; Kou, L.; Huang, A.; Gao, H.; Lin, Z.; Xie, Y.; Zhang, L. Comparison and Synthesis of Precipitation Data from CloudSat CPR and GPM KaPR. *Remote Sens.* **2024**, *16*, 745. https://doi.org/10.3390/rs16050745

Academic Editor: Kenji Nakamura

Received: 16 January 2024
Revised: 11 February 2024
Accepted: 18 February 2024
Published: 21 February 2024

1. Introduction

An accurate characterization of global precipitation is indispensable for improving global climate and weather forecasting models, as well as for evaluating the global energy budget and water resources [1]. Clouds play an important role in the hydrological cycle, redistributing water and generating precipitation on a global scale. To thoroughly comprehend the significance of clouds and precipitation, and to enhance their performance in numerical models, it is crucial to obtain global-scale measurements of these phenomena and conduct detailed investigations into their formation, development, and dissipation processes across all scales [2]. Microwave sensors outperform infrared and visible-light sensors in precipitation retrieval, since they exhibit higher sensitivity to rain and ice parti-

cles [3]. Moreover, active microwave cloud and precipitation radars have the advantages of strong penetration and high accuracy of precipitation estimation [4].

The CloudSat satellite equipped with a W-band cloud profiling radar (CPR) can quantitatively measure the vertical structure of clouds and precipitation [5]. The Global Precipitation Measurement Mission (GPM) core satellite carries a dual-frequency precipitation radar (DPR) operating in the Ku band and Ka band [6]. DPR can provide measurements of the 3D precipitation structure on a global scale. Owing to differences in orbital inclinations, the CloudSat satellite and the GPM satellite occasionally intersect, thereby affording an opportunity for multi-frequency precipitation measurement.

Conducting a comparative study on precipitation measurement using radar systems operating at different bands is of paramount importance in order to harness and integrate the unique strengths of each band. In conjunction with the CloudSat CPR, Berg et al. (2010) utilized the Tropical Rainfall Measuring Mission (TRMM) precipitation radar (PR) to assess rainfall distribution and intensity in tropical and subtropical oceans [7]. Their results indicated that CPR detected rainfall occurrences nearly 2.5 times more frequently than TRMM PR. Tang et al. (2017) conducted a global-scale evaluation by matching TRMM PR, GPM dual-frequency precipitation radar (DPR), and CloudSat CPR data [8]. Sindhu et al. (2017) compared the reflectivity derived from CloudSat CPR and TRMM PR by analyzing their coincident events [9]. The results demonstrated that the reflectivity from CloudSat CPR was approximately 10 dBZ lower than that of TRMM PR below a height of 4 km. Fall et al. (2013) analyzed the vertical structure of storms utilizing data from CloudSat CPR, TRMM PR, and ground-based radar [10]. They further conducted multi-frequency measurements of microphysical quantities within different regions of the melting layer and carried out comparisons among them. This study revealed the characteristics of the bright band in cold-season precipitation and its impact on radar-based quantitative precipitation estimation. CloudSat CPR exhibited excellent sensitivity in detecting snow, whereas GPM KaPR, as a supplemental payload designed to compensate for the limitations of the Ku band in detecting snow, ice, and light rain, also demonstrated robust snow detection capabilities. The ability of DPR to identify snowfall was evaluated by utilizing a dataset with observation intervals of less than 5 min between DPR and CPR [11]. Mroz et al. (2021) compared surface snowfall rates estimated by GPM DPR and CloudSat CPR with estimates derived from multi-radar and multi-sensor composite products covering the continental United States from November 2014 to September 2020 [12]. Skofronick-Jackson et al. (2019) compared three years of CPR and DPR snowfall data, taking into account differences in hardware, inversion algorithms, and radar bands. It was found that the global average near-surface snowfall accumulation in DPR was about 43% lower than that in CPR [13].

The Ka- and W-band spaceborne radars possess different advantages in the measurement of precipitation structures. The higher frequency of the W-band radar enables it to achieve superior spatial resolution and sensitivity, capturing detailed cloud structure and light precipitation. Conversely, the relatively lower frequency of the Ka-band radar allows for partial penetration of clouds and precipitation, facilitating the accurate measurement of light-to-heavy precipitation. The integration of these two radar bands yields complementary information, fostering a more comprehensive understanding of precipitation cloud characteristics. Notably, NASA's Aerosol/Cloud/Ecosystems (ACE) mission incorporates dual-band and dual-polarization modes in the W and Ka bands to enhance the functionality and performance of cloud radar [14,15]. Currently, China has successfully launched its first spaceborne precipitation radar, and the National Satellite Meteorological Center is planning the deployment of a cloud measurement satellite. The primary payload under consideration for this initiative is a W- and Ka-band measurement radar [16].

In this paper, we compare and synthesize precipitation data obtained by CPR-KaPR coincidence datasets. To begin with, we match the precipitation observations from both radars in terms of space and time. Next, we compare the differences in precipitation measurement between the two radar systems, including radar reflectivity, as well as the spatial distribution and intensity of the near-surface precipitation rate with different phases.

Finally, we synthesize the radar data from the two bands to obtain a more complete and comprehensive vertical structure of precipitation.

2. Data and Matching Methods

2.1. CloudSat CPR Data

The CloudSat satellite carries the most widely used spaceborne cloud radar, known as millimeter-wave cloud profiling radar (CPR). CPR is a W-band radar that is pointed toward the nadir and has a minimum detectable signal of approximately −29 dBZ. The radar footprint size is 1.7 km along-track and 1.4 km cross-track, while the vertical resolution is about 500 m [17,18].

In this study, we utilize radar bin data with a cloud mask value of 40, indicating a high confidence level in cloud identification [19,20]. The retrieval process for near-surface precipitation rates accounts for factors such as radar beam attenuation, multiple scattering effects, and precipitation identification in the ground clutter region (the five lowest radar bins above the surface, approximately 1.2 km) [21]. Retrieval of near-surface precipitation rates relies on radar reflectivity and the estimated value of path-integrated attenuation (PIA), which are determined based on surface reflectance characteristics. However, due to the complex nature of land surface reflectance compared to that of the ocean, retrieval of precipitation data over land surfaces is not feasible [22].

For snowfall products, the backscattering characteristics of snow particles are calculated using a combination of the original model for small particles and an aggregation model for large particles [23]. Assuming an exponential particle size distribution for snow, the slope and intercept parameters of the particle size distribution are obtained through the application of the optimal estimation method [24]. This optimization method minimizes a cost function that represents the weighted sum of differences between simulated and observed radar reflectance, as well as the disparities between prior and estimated microphysical properties of snow. Ultimately, the retrieved particle size distribution parameter curve allows for the derivation of snowfall estimates.

For this research, we used a variety of parameters, such as the radar reflectivity factor, cloud scene, near-surface rain rate, snowfall rate, and others. These parameters were derived from the 2B-GEOPROF, 2C-PRECIP-COLUMN, and 2C-SNOW-PROFILE products. These products were specifically extracted from the CloudSat Version 5 data release by the CloudSat data team in 2019.

2.2. GPM KaPR Data

The GPM is a new generation of precipitation observation program following the TRMM. Its core satellite carries two instruments for measuring precipitation: the GPM Microwave Imager (GMI), and the DPR. One goal of the DPR is to measure light-to-heavy precipitation using Ka-band (35.5 GHz) radar (KaPR) and Ku-band (13.6 GHz) radar (KuPR) [25]. This study uses KaPR HS-mode data because the Ka-band HS mode is more sensitive than that of the Ku-band. In addition to detecting more occurrences of light precipitation, it can also detect more clouds. The scanning angle range of the KaPR antenna is $\pm 8.5^{\circ}$, the vertical resolution is 500 m for KaHS, the scanning width is 120 m, and the spatial resolution is 5 km. The minimum detectable reflectivity of KaPR is 10.40 dBZ, corresponding to the minimum detectable precipitation rate of 0.16 mm/h [26]. The technical indicators of KaPR and CPR are shown in Table 1.

The Ka-band data used in this paper were the standard 2A-DPR High-Sensitivity Mode (HS) product of GPM DPR L2 version 7, which were obtained by attenuation correction and non-uniform filling correction based on level L1 base data [26].

Table 1. Brief description of CPR and KaPR.

Instrument	CloudSat CPR	GPM KaPR
Launch time	18 April 2006	27 February 2014
Inclination angle (°)	98.23	65
Altitude (km)	705	407
Frequency (GHz)	94	35
Vertical resolution (m)	500	500 (KaHS)
Along-track resolution (km)	1.7	5
Cross-track resolution (km)	1.4	5
Minimum detectable Ze (dBZ)	−29	10.40 (KaHS)

2.3. Data Matching and Coincidence Data Processing

Before comparing the datasets generated by the two radar systems, a requirement lies in the alignment and time synchronization of their measurements. Within this context, the term "coincident event" assumes paramount importance, signifying a conjunctive occurrence of radar pixels. The critical criterion for a coincident event hinges upon time and location, stipulating that the coincidence between the footprints of the two radar systems must be within 15 min. To initiate this process, it is imperative to query the KaPR data associated with the footprint, within the specified 15-min window, predicated upon the transit time of the CPR. In instances where the trajectories of the footprint indeed coincide, recourse should be made to the nearest-neighbor methodology [27]. This approach facilitates the judicious amalgamation of the two radar datasets, thereby yielding the coveted CPR-KaPR coincidence data. The time difference threshold of 15 min has very little impact on the accuracy of the statistical results [28]. We chose 15 min by considering the trade-off between the number of samples and the time difference and statistical accuracy.

Following the spatiotemporal matching methodology delineated earlier, it can be discerned that, due to the superior footprint resolution exhibited by the CPR as compared to the KaPR, multiple observations of the footprint by the CPR are found to correspond to a single footprint observation by KaPR, as visually illustrated in Figure 1a. To rectify this disparity and establish a one-to-one correspondence between the CPR and KaPR pixel values, a resampling procedure was executed along the trajectory of the CPR orbit. Under the assumption of a uniform distribution of cloud features along the direction of the CPR orbit, the pixel values of the CPR data were spatially averaged within each corresponding KaPR pixel. In this manner, the mean values encompassing C2 to C4 correspond to C1′, while the mean values spanning C5 to C8 correspond to C2′. For the value of KaPR footprints, Kn = Kn′. KaPR footprints designated with primed symbols in Figure 1b serve the purpose of distinguishing data before and after the resampling process. The post-resampling dataset maintains parity with the KaPR dataset in terms of volume, and it is visually depicted in Figure 1b.

Following the rigorous data resampling process, a substantial dataset comprising a total of 310,095 sets of CloudSat CPR and GPM KaPR coincident events was successfully collated, spanning from March 2014 to December 2017. Within this illustrative representation, the dots serve to delineate the trajectory of the coincident orbit, with the depth of color encoding the corresponding coincident frequency, as shown in Figure 2. It is imperative to underscore that, owing to the disparate inclination angles governing the orbits of the two satellites, a notable variation in coincident frequency can be discerned across distinct latitudinal bands. Notably, within the geographical expanses spanning 55 to 67 degrees (north and south latitudes), the coincident frequency registers a noteworthy augmentation, ranging from 50% to an impressive 800% higher than observed at other latitudinal coordinates.

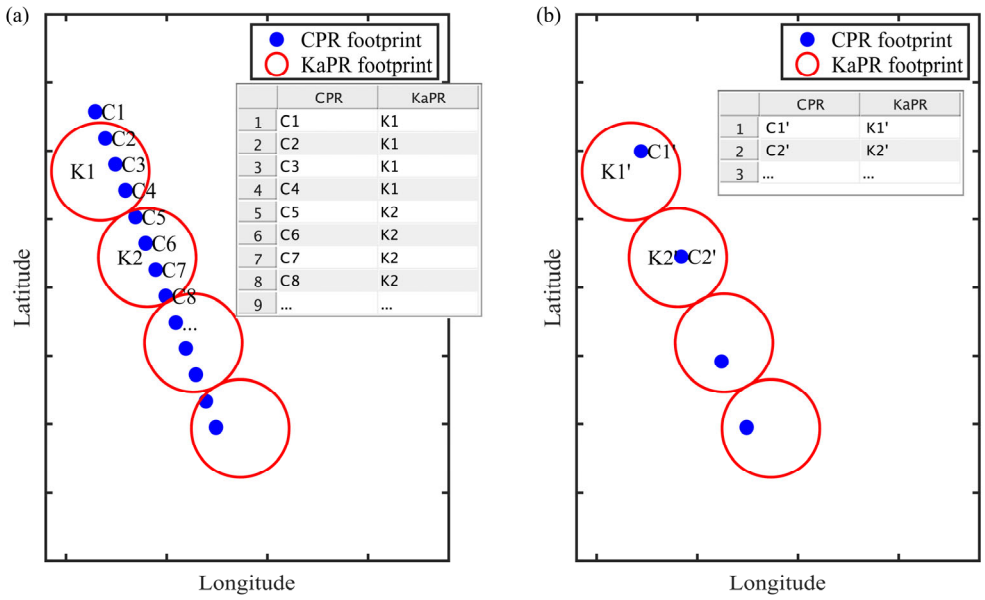

Figure 1. Resampling diagram ((**a**): data before resampling, (**b**): data after resampling).

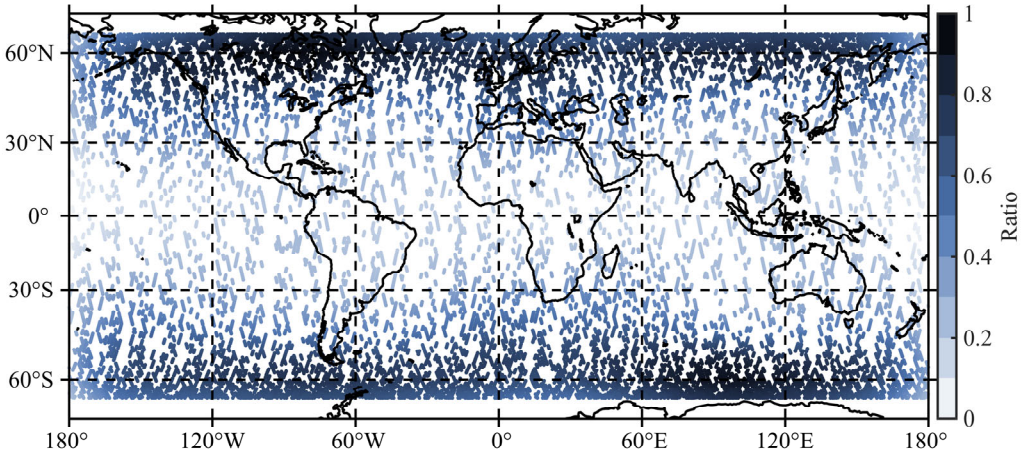

Figure 2. Footprints of CPR and KaPR coincident events between March 2014 and December 2017.

3. Results

3.1. Comparison of Reflectivity

Radar systems operating in distinct bands exhibit differences in their precipitation measurements. These disparities arise from the frequency-dependent nature of precipitation's microphysical characteristics, leading to differential scattering or absorption responses among radars operating in dissimilar frequency ranges. Through a comparative analysis of radar reflectivity across various frequency bands, it becomes possible to discern and investigate the sensitivity differentials exhibited by radars in response to different precipitation types.

In this study, the classification of precipitation phases within the study area relied upon the near-surface precipitation phase parameters from the KaPR. Specifically, footprints wherein both the CPR and the KaPR detected liquid-phase precipitation were designated as "rainfall footprints". Conversely, those footprints characterized by solid-phase precipitation were categorized as "snowfall footprints". When KaPR could not identify near-surface precipitation due to sensitivity reasons, we chose to trust CPR's precipitation phase identification. After identification, a total of 12,126 rainfall footprints and 14,737 snowfall footprints were selected. Given the greater precision of KaPR in discerning the bright band phenomenon, the classification of rain types within the rainfall footprints primarily hinges on the near-surface rain type parameters obtained from KaPR. Footprints identified by

KaPR as indicative of convective rainfall were designated as "convective rainfall footprints". Subsequently, those footprints identified by KaPR as representing stratiform rainfall were categorized as "stratiform rainfall footprints". This classification process yielded a final count of 4670 convective rainfall footprints and 7456 stratiform rainfall footprints.

Figure 3 presents a two-dimensional probability distribution diagram illustrating the radar reflectivity–height relationship for convection, stratiform rainfall, and snowfall during intersecting events observed by the CPR and the KaPR. Figure 3a–c depict the radar reflectivity–height profiles for CPR convection, stratiform rainfall, and snowfall, respectively. Subsequently, Figure 3d–f display the two-dimensional probability distribution images of radar reflectivity–height for KaPR convection, stratiform rainfall, and snowfall, respectively. In these representations, the abscissa denotes the radar reflectivity, the ordinate signifies the altitude, and the color mapping indicates the probability of observing a particular radar reflectivity at a given altitude in different precipitation types. The figure reveals distinctive patterns among the precipitation types. In convective rainfall, most CPR reflectivity between altitudes of 1.5 and 5 km exhibits a decreasing trend as altitude decreases, reflecting the presence of larger liquid particles with more pronounced attenuation of W-band radar waves. Conversely, most KaPR reflectivity gradually increases with decreasing altitudes during convective rainfall. For stratiform rainfall, both CPR and KaPR reflectivity between altitudes of 1 and 4 km remains relatively stable. CPR reflectivity primarily falls within the range of 7–12 dBZ, while KaPR reflectivity is predominantly distributed between 16–21 dBZ. This phenomenon arises from the stable intensity of stratiform rainfall and the larger size of liquid particles compared to convective rainfall.

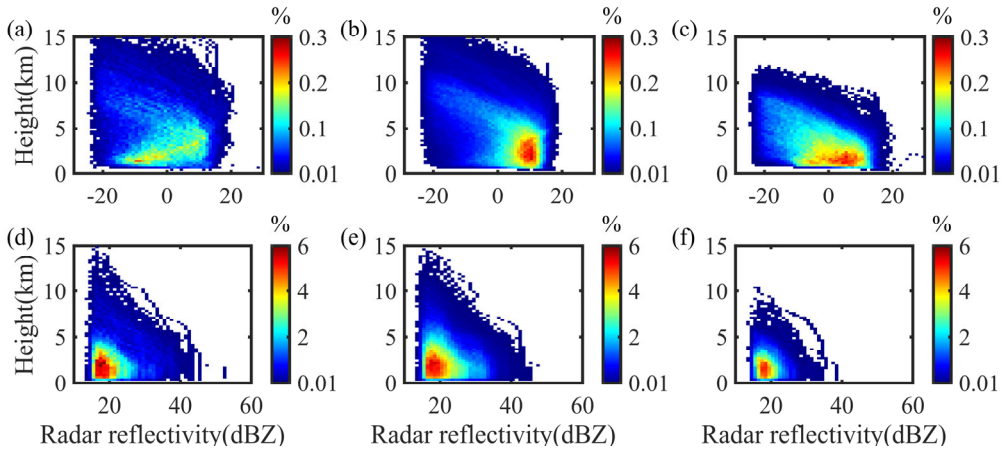

Figure 3. Reflectivity–height two-dimensional (2D) probability distribution of convective rain, stratiform rain, and snow in CPR-KaPR coincidence ((**a**): CPR convective rain; (**b**): CPR stratiform rain; (**c**): CPR snow; (**d**): KaPR convective rain; (**e**): KaPR stratiform rain; (**f**): KaPR snow).

Furthermore, the figure highlights variations in the two-dimensional probability distribution images between snowfall and rainfall, with CPR exhibiting more pronounced characteristics compared to KaPR. This divergence can be attributed to the higher frequency of the W band, which results in greater scattering efficiency in smaller water droplets and ice crystals. Such small particles are prevalent during snowfall, contributing to the broader radar reflectivity–height distribution exhibited by CPR during snowfall events. Consequently, W-band radar can offer more detailed structural information regarding snowfall events.

Regarding echo height, the average echo-top heights observed in convective rainfall, stratiform rainfall, and snowfall were as follows: for the CPR, they measured 7.56 km, 8.16 km, and 6.70 km, respectively, whereas for the KaPR, the average echo-top heights were 3.92 km, 4.11 km, and 3.08 km, respectively. Notably, the average echo-top heights detected by CPR exceeded those detected by KaPR, by approximately 3.6 to 4.2 km on average. This discrepancy arises due to CPR's superior resolution, which enables it to

detect smaller cloud particles and provides a more comprehensive vertical profile of cloud particle information.

Figure 4 displays the average radar reflectivity profiles for convective rainfall, stratiform rainfall, and snowfall during the coincident event. The horizontal error bars in the figure are one standard deviation of the average radar reflectivity at each corresponding altitude. The observations reveal distinct performance in different regions:

1. In the lower region, below 1 km altitude, within convective rainfall, both CPR and KaPR exhibit a gradual increase in average reflectivity with decreasing altitude. This phenomenon arises due to the relatively lower attenuation of W-band radar waves in this region compared to the increase in the detection values.
2. In the altitude range of 1.5 to 5 km, the reflectivity for most CPR observations within convective rainfall exhibits variations with altitude, while KaPR observations show the opposite trend. This difference can be attributed to the substantial attenuation of W-band radar waves, which is more pronounced than the corresponding increase in detection values in this altitude range.
3. Within stratiform rainfall, the CPR average reflectivity initially increases and then decreases as the altitude rises between 1 and 3 km. In contrast, the KaPR reflectivity gradually decreases with increasing altitude in the same altitude range. This behavior can be attributed to the greater attenuation of W-band radar by liquid particles between 1 and 3 km, resulting in a reduction in the average reflectivity. While Ka-band electromagnetic waves also experience attenuation, their average attenuation is less pronounced than the corresponding increase in reflectivity. Hence, the average profile value for CPR gradually decreases with decreasing altitude, whereas the average profile value for KaPR increases with decreasing altitude.
4. In the case of snowfall, the average reflectivity profile of the CPR exhibits more pronounced variations with height compared to that of the KaPR, with a notable peak occurring near the altitude of 10 km. This divergence can be attributed to the heightened sensitivity of the W band, which enables the CPR to detect more detailed snow features that fall below the detection threshold of the KaPR. Consequently, the CPR reveals more gradients in reflectivity, offering a more comprehensive characterization of snowfall particle features.

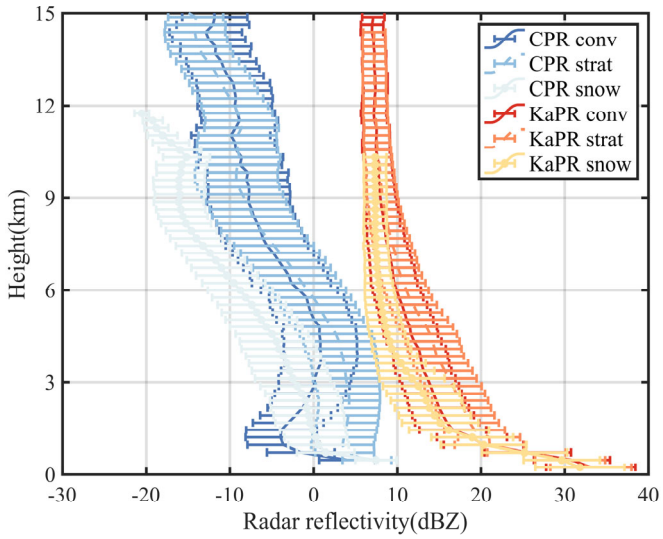

Figure 4. Average profiles of radar reflectivity for convective rain, stratiform rain, and snow in CPR and KaPR coincident events.

From Figures 3 and 4, we contend that the reflectivity measurements by cloud and precipitation radars operating in different bands can effectively complement one another. The W-band radar, with its higher spatial resolution and sensitivity, can provide light

precipitation and cloud structure details, whereas the Ka-band radar excels in its ability to mitigate signal attenuation, allowing it to penetrate thick cloud cover and measure light-to-high precipitation. By comparing the radar reflectivity from the two bands, we found that the joint measurements are complementary and can expand the vertical structure range of precipitation clouds. Considering the continuity of precipitation, future advancements in precipitation algorithms could benefit from incorporating additional upper-level cloud information as constraints in the precipitation estimation process.

3.2. Comparison of Near-Surface Precipitation

In addition to assessing the vertical structure measurement of the two radars, it is essential to conduct a global-scale comparison of the near-surface precipitation data retrieved by them. This comprehensive evaluation will provide insights into their capabilities for assessing and monitoring precipitation across various regions and varying intensity levels.

3.2.1. Comparison of Rain Rates

In the comparison of near-surface rain rates, it is crucial to consider that the retrieval process for near-surface precipitation using the CPR takes into account factors such as attenuation and multiple scattering effects of radar beams, as well as the identification of precipitation in areas with ground clutter. This retrieval process involves utilizing data related to near-surface radar reflectivity and surface reflection characteristics. Path-integrated attenuation estimates are then employed to retrieve near-surface rain rates. Due to the inherent complexity of land surface albedo in contrast to the ocean, it is not feasible to retrieve precipitation data over land surfaces. Consequently, our comparison is limited to the assessment of ocean surface rainfall data retrieved by both radar systems.

For statistical purposes in the coincident event, all footprints reporting rain were selected, as it is important to note that the CPR can detect rainfall of lower intensity compared to the KaPR. Consequently, there may be instances where the CPR detects rainfall while the KaPR does not, resulting in cases where the CPR has a non-zero retrieval value while the KaPR records a value of 0 for near-surface rain rate.

To assess the performance of the two radars in rainfall estimation across diverse global regions, Figure 5 presents the average near-surface rain rate distribution based on coincident events observed by the two satellite-borne radars. The resolution for this analysis is 5 degrees * 5 degrees. Specifically, Figure 5a,b illustrate the average near-surface rain rate distributions for CPR and KaPR, respectively. Figure 5c depicts the distribution of the average near-surface rain rate differences between the two radars. The boxplot of the average near-surface rain rate between the two radars, with 40 degrees latitude as the boundary, is shown in Figure 5d.

The findings reveal that, within the latitudinal range of 40 degrees north and south, the average near-surface rainfall retrieved by KaPR is 0.4 mm/h greater than that retrieved by CPR. Conversely, above 40 degrees north and south, the average value retrieved by CPR surpasses KaPR by 0.1 mm/h. This variation suggests that, at low latitudes, the impact of heavy rainfall is more pronounced, leading to greater attenuation of CPR's electromagnetic waves. Consequently, CPR may struggle to accurately estimate rainfall exceeding its upper threshold, resulting in a lower average rainfall retrieval compared to KaPR. In addition to the fact that the probability of heavy precipitation events at high latitudes is smaller than that at low latitudes, as the latitude increases, the sampling frequency gradually increases, and the proportion of cases where there is a large difference in the retrieval values between the two also decreases. At high latitudes, there is a prevalence of medium- and small-intensity rainfall events compared to mid-latitudes. CPR's heightened sensitivity allows it to detect 15% more rainfall than KaPR in such conditions.

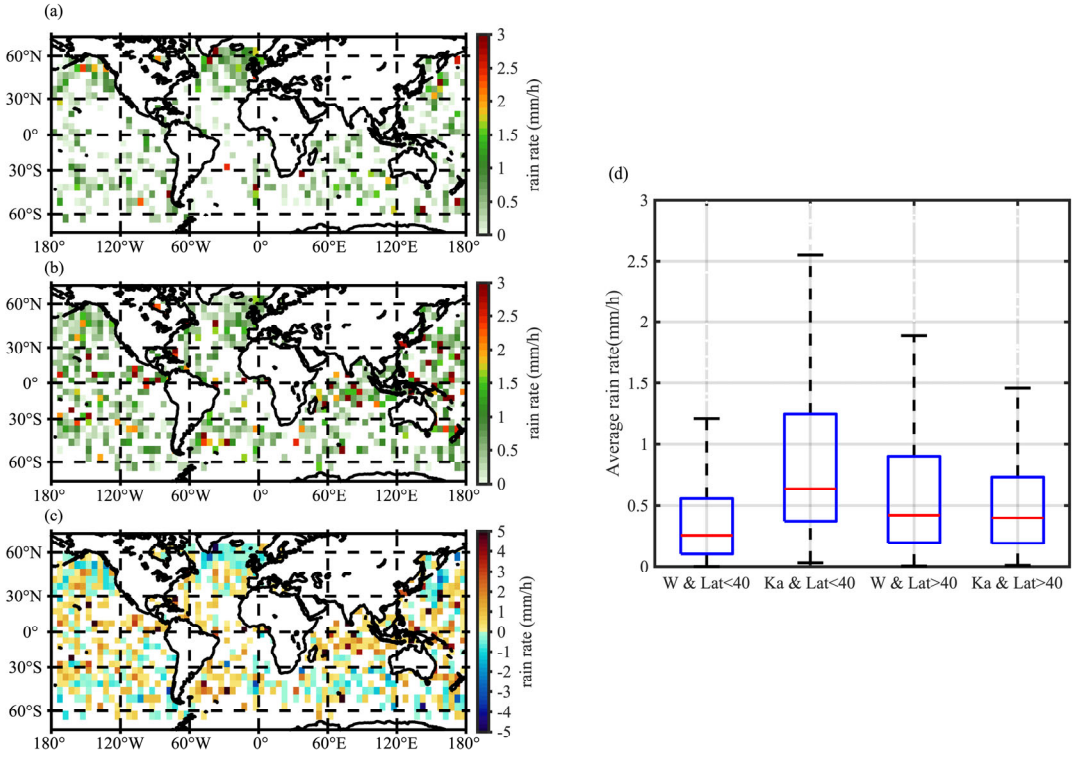

Figure 5. Average near-surface rain rate distribution based on coincident events ((**a**): CPR, (**b**): KaPR, (**c**): average near-surface rain rate difference between the two, (**d**): boxplot of the average near-surface rain rate between the two).

After comparing the rainfall detection capabilities of the two radars across different regions, we proceeded to evaluate their performance in near-surface rainfall of varying intensities. We selected footprints with rainfall retrieval values from both radar systems for this comparison. Figure 6a presents a scatter probability distribution of the near-surface rainfall rates observed by the CPR and the KaPR during coincident events. The majority of the rainfall events detected by both radar systems fall within the range of 0.2 to 1 mm/h.

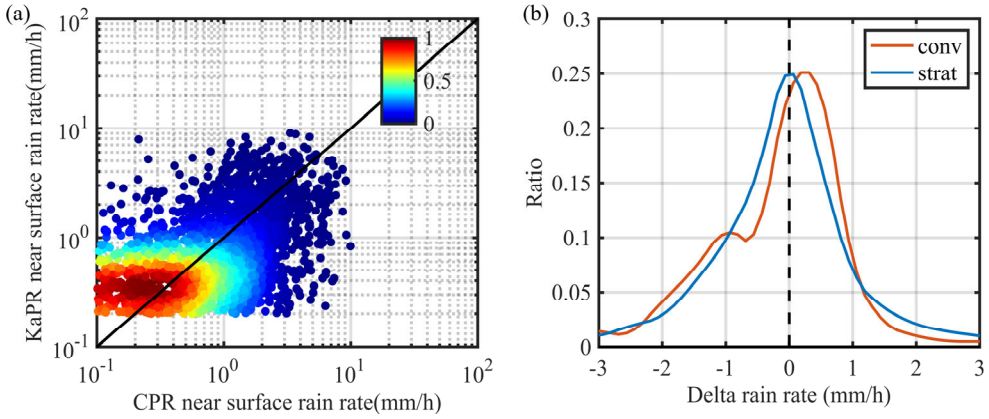

Figure 6. (**a**) CPR and KaPR near-surface rain rate scatter probability distribution and (**b**) convective and stratiform rain rate difference frequency distribution (Δrain rate = KaPR rain rate—CPR rain rate).

To quantify the agreement between the two radar systems in terms of near-surface rain rate, we calculated the correlation coefficient (CC) and the root-mean-square error (RMSE) for the inversion results. The overall correlation coefficient for the near-surface rain rate retrieved by both radars was 0.4, while the root-mean-square error was 2.18 mm/h.

These metrics suggest a moderate level of correlation and an average level of agreement between the near-surface rain rate estimates obtained from the two radar systems.

To analyze the differences in the near-surface rain rate values simultaneously retrieved by both radars, we categorized these differences based on whether the precipitation was convective or stratiform. Subsequently, we compiled and tabulated the frequency distribution of the differences between the near-surface rain rates derived from the CPR and the KaPR, as illustrated in Figure 6b.

Figure 6b reveals that the differences in near-surface rainfall between the CPR and KaPR follow a Gaussian distribution. Specifically, during convective rainfall events, the KaPR tends to produce higher values compared to the CPR. In contrast, during stratiform rainfall events, the differences between the two radar systems follow a standard normal distribution with a mean of zero.

We attribute these findings to the characteristics of convective and stratiform precipitation. In convective rainfall, precipitation cloud clusters are typically thicker, and near-surface precipitation particles tend to be larger. The CPR near-surface rain rate algorithm may underestimate the attenuation of W-band radar waves in such conditions, resulting in lower average near-surface rain rate estimates compared to KaPR.

On the other hand, stratiform rainfall tends to be more stable. In these conditions, the attenuation of W-band radar waves is less pronounced compared to convective rainfall. While W-band electromagnetic waves do experience substantial attenuation in cases of heavy stratiform rainfall, they may provide more accurate estimates of near-surface rain rates during periods of lower-intensity precipitation. Hence, for stratiform rainfall, differences between the two radars tend to conform to a standard normal distribution.

Numerous factors contribute to the disparities in near-surface rain rate retrieval between the CPR and the KaPR. These encompass distinct retrieval algorithms employed by the radars, as well as the influence of radar electromagnetic wave refraction and multiple scattering phenomena during the detection process. CPR and DPR employ different microphysical assumptions and retrieval algorithms, which is also an important factor influencing differences in rain rate. Based on the comparison of reflectivity and near-surface rain rate between the two radars, due to the attenuation of CPR, the difference in near-surface rain rate may also be related to the change in reflectivity in the vertical direction.

To illustrate the relationship between the change in reflectivity in the vertical direction and near-surface rainfall, we introduced a parameter linked to the gradient of the radar reflectivity. When the radar reflectivity within this frequency increases with decreasing altitude, a value of 1 is assigned to the bin, while a value of -1 is assigned when the reflectivity decreases with altitude. This procedure enables the derivation of the radar reflectivity gradient profile specific to the precipitation cloud within this frequency. The gradient profile difference across the entire precipitation cloud was computed by subtracting the radar reflectivity gradient profiles of KaPR and CPR. Figure 7a provides a schematic diagram depicting this process.

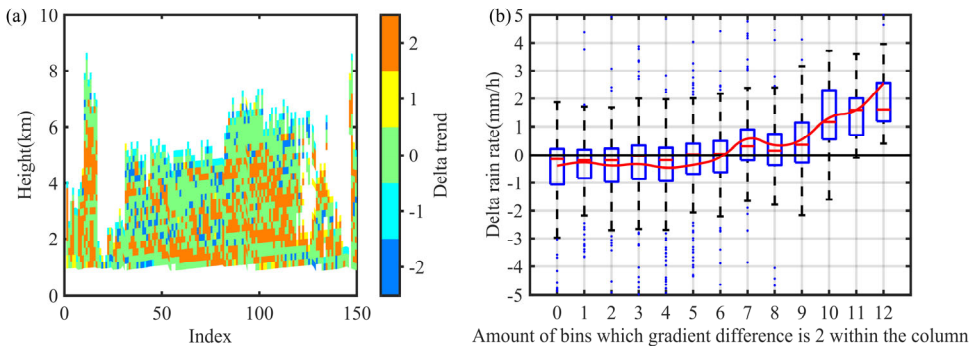

Figure 7. (**a**) Schematic diagram of the gradient profile difference of KaPR and CPR radar reflectivity of precipitation clouds, and (**b**) the boxplot of the delta near-surface rain rate and amount of bins whose gradient difference is 2 within the column.

When the radar reflectivity of both radars exhibits the same trend as altitude decreases, the resulting profile difference is 0. However, during heavy rainfall, the KaPR reflectivity gradually increases with decreasing altitude, while the CPR reflectivity undergoes attenuation due to raindrop particles, leading to a gradual decrease with decreasing altitude. Consequently, the profile difference reaches a value of 2. We proceeded to tally the number of data bins where the difference between the radar reflectivity gradient profiles of precipitation clouds derived from KaPR and CPR equaled "2". This count is presented in Figure 7b, in the form of a boxplot, alongside the near-surface rain rate difference.

The boxplot reveals that when the amount of bins exhibiting a difference of "2" surpasses or equals six within the column, the average near-surface rain rate retrieved by CPR is smaller than that obtained by KaPR. When the count of bins with a profile difference equal to "2" reaches or exceeds 10, CPR consistently yields smaller average near-surface rain rates compared to KaPR. Additionally, the average near-surface rain rate difference varies commensurately with the count of bins exhibiting a profile difference of "2". These findings underscore that, at a certain level of rainfall rate, the attenuation of W-band radar waves cannot be accurately estimated, resulting in the underestimation of the near-surface rain rate by CPR.

3.2.2. Comparison of Snowfall Rates

Snowfall is the meteorological phenomenon characterized by the descent of ice crystals from the atmosphere to the Earth's surface, forming snow. This process signifies the atmospheric transfer of water to the surface, constituting an integral component of the natural water cycle [29]. In the context of precipitation comparisons, it is important to conduct a global-scale evaluation of near-surface snow rates retrieved by the two radar systems.

The average distribution of near-surface snow rates retrieved by the CPR and the KaPR is illustrated in Figure 8a,b, respectively. Meanwhile, Figure 8c displays the distribution of the average near-surface snow rate difference between the two radar systems. The boxplot of the average near-surface snow rate between the two radars, with 50 degrees latitude as the boundary, is shown in Figure 8d. It is noteworthy that the CPR snow rate algorithm truncates the reflectivity profile at an altitude of approximately 1 km to mitigate the impact of ground clutter [30]. Consequently, in regions characterized by terrain-related factors between 30 and 50 degrees (north and south latitudes), CPR's inversion values tend to be lower than those of KaPR. Figure 8c illustrates this phenomenon, with specific regions such as the Tibetan Plateau in mainland China, the Rocky Mountains in the Western United States, and the Cordillera Mountains in South America exhibiting lower near-surface snow rate inversion values for CPR compared to KaPR. However, CPR's heightened sensitivity enables it to detect a greater number of snowfall events than KaPR in areas with latitudes exceeding 50 degrees, accounting for 86% of the total snowfall events.

The discrepancy in radar wave frequencies results in a deviation of several hundred meters in the selected sampling heights for the two near-surface snow rate algorithms near the ground. Therefore, KaPR tends to yield higher snow rates, attributed to terrain-related factors, compared to CPR. Nevertheless, CPR's advantage in terms of high sensitivity allows it to detect more snowfall events in high-latitude regions than KaPR.

Apart from terrain-related factors, as shown in Figure 8d, the average near-surface snow rate retrieved by KaPR in areas below 50 degrees (north and south latitudes) exceeds that of CPR by 0.2 mm/h. Conversely, in regions above 50 degrees (north and south latitudes), the average near-surface snow rate retrieved by CPR surpasses that of KaPR by 0.1 mm/h. This discrepancy arises because CPR detects 45% more light snow events (with intensities in the order of 0.01 mm/h) than KaPR in regions above 50 degrees (north and south latitudes).

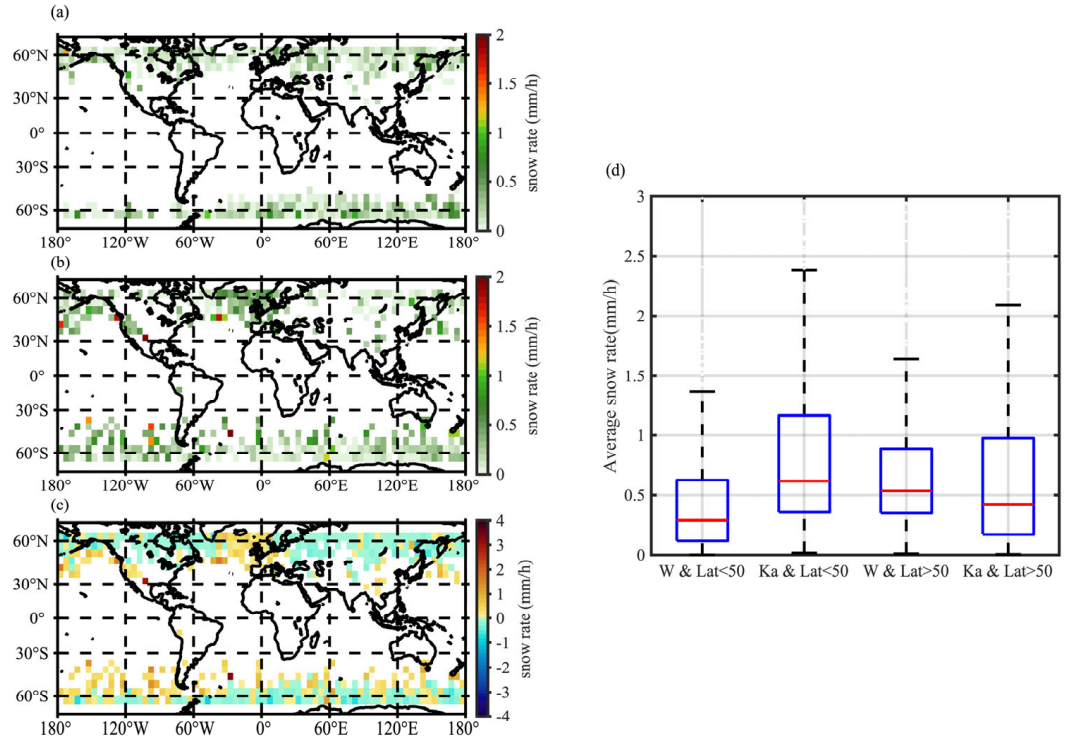

Figure 8. Average near-surface snow rate distribution based on coincident events of two spaceborne radars ((**a**): CPR, (**b**): KaPR, (**c**): difference in average near-surface snow rate, (**d**): boxplot of the average near-surface snow rate between the two).

4. Precipitation Synthesis from CPR and KaPR

The comparative analysis of near-surface precipitation between the two radar systems reveals that CPR excels in detecting weaker precipitation compared to KaPR. For heavier precipitation, the W-band radar waves experience attenuation, leading to an underestimation of precipitation by CPR. The KaPR has the advantage in detecting light-to-heavy precipitation.

Combining the near-surface precipitation data retrieved by both radar systems involves considering instances where one or both radars retrieve near-surface precipitation. In cases where both radars detect near-surface precipitation simultaneously, the maximum value is selected for inclusion in the statistics, resulting in a maximum near-surface rain rate dataset. The frequency distribution statistics of near-surface precipitation rates in coincident events for both radar systems are presented in Figure 9.

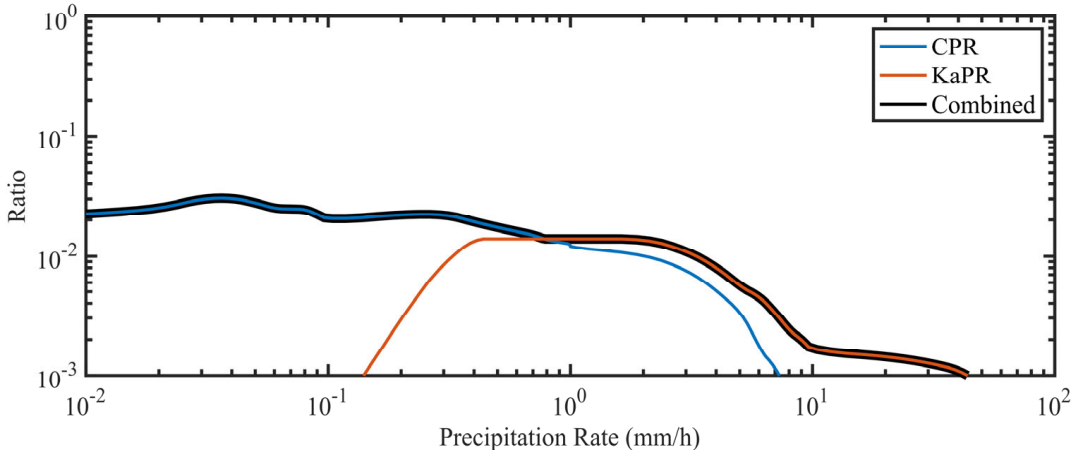

Figure 9. Frequency distribution of near-surface precipitation rates of CPR and KaPR coincident events.

In Figure 9, the x-axis indicates the precipitation rate, while the y-axis indicates the occurrence frequency. The blue and orange lines indicate the frequency of precipitation at different intensities detected by CPR and KaPR, respectively. The black lines indicate the near-surface precipitation rates obtained from the maximum combination of the two radar datasets. The observed trends in Figure 9 are as follows:

1. In the precipitation rate range of 0.01–0.2 mm/h, KaPR, due to its sensitivity limitations, is unable to detect precipitation within this range.
2. In the rate range of 0.2–8 mm/h, as precipitation rate increases, the near-surface rain rate retrieved by the CPR gradually underestimates, leading to a decrease in the proportion of CPR-detected precipitation and an increase in the proportion of KaPR-detected precipitation.
3. When the precipitation rate exceeds 7 mm/h, the values retrieved by CPR are smaller than those retrieved by KaPR.

This analysis demonstrates that the combined detection of near-surface precipitation by both radar systems allows for a more complete detection of precipitation, with rates ranging from 0.01 to 40 mm/h or higher levels.

In addition to the synthesis of near-surface precipitation, we also synthesized reflectivity cross-sections to better represent the vertical structures of precipitation clouds. Based on the previous analysis of the comparison of reflectivity, near-surface precipitation, and the reflectivity gradient, we adopted a weighted synthesis method associated with the reflectivity gradient difference to synthesize the reflectivity in the vertical cross-sections. Figure 10 illustrates the flowchart of synthesizing radar reflectivity from both radars. The following steps outline this synthesis procedure: Firstly, import both radar datasets and subject them to quality control measures. Secondly, calculate the vertical gradient of the radar reflectivity for each footprint. In this calculation, assign a value of 1 to the bin gradient where the radar reflectivity increases with decreasing altitude. Conversely, assign a value of -1 to the radar bin gradient where the radar reflectivity decreases with decreasing altitude. Thirdly, subtract the gradient value of the W band from the gradient value of the Ka band to derive the gradient difference for each bin. Since the reflectivity of the two radars changes differently as the altitude decreases, the value of the gradient difference of each bin may be any integer between the values of -2 and 2. When bins with a gradient difference equal to 2 appear continuously within a footprint, it means the occurrence of precipitation above the CPR measurement threshold. We assigned a synthetic weight factor "k" to each bin based on the total number of gradient differences equal to 2 in the vertical direction of the footprints. It can be seen from Figure 7b that when the total number of bins with a gradient difference equal to 2 in the footprints reaches 10, the precipitation rates estimated by CPR are smaller than those estimated by KaPR. When bins with a gradient difference equal to 2 appear continuously, the "k" of the top bin is assigned a value of 0.9. Then, "k" decreases in height by 0.1 with each successive bin featuring a gradient difference equal to 2, until reaching a value of 0. Finally, the composite reflectivity is obtained from both frequencies with a weighted average method incorporating the gradient information.

Due to scattering differences caused by different bands, the synthesis process involves simulating the scattering of electromagnetic waves in both the W and Ka bands when interacting with solid, mixed, and liquid particles. This step refers to the simulation method in Kou's [31] work, but the types of particles are not divided in detail in this synthesis. We simply classified particles into ice, mixed, and liquid. The "Ice" bins were referenced to cloud ice for scattering simulation, the "mix" bins were referenced to wet snow for scattering simulation, and the "liquid" bins were referenced to raindrop particles for scattering simulation. This simulation helped establish the conversion relationship of radar reflectivity between the W and Ka bands. Subsequently, based on the phase parameters provided by KaPR, the reflectivity factor Ze_W in the W band was converted to the Ka-band radar reflectivity factor $Ze_{W\text{-}Ka}$.

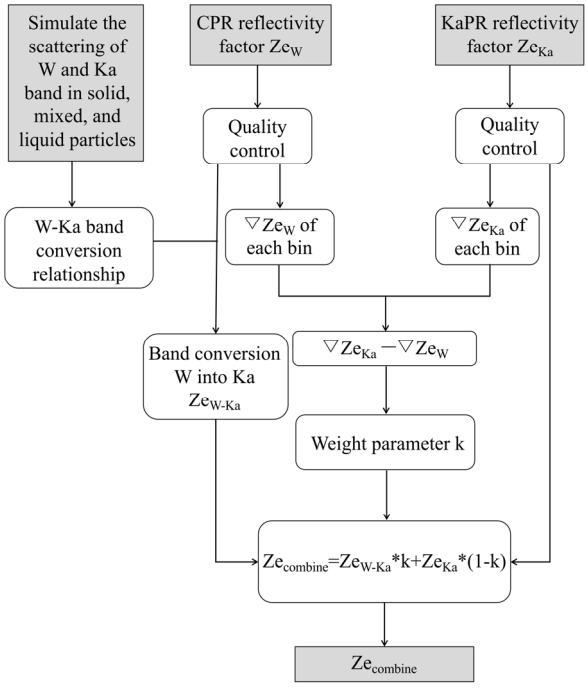

Figure 10. Flowchart of CPR and KaPR reflectivity synthesis.

The final step in this process is the calculation of the composite reflectivity $Ze_{combine}$ for each bin, incorporating the composite weight factor k. Specifically, when only a single radar detects clouds within a bin, the reflectivity factor value of that radar is used. Conversely, when both radars detect clouds simultaneously, the synthesized reflectivity $Ze_{combine}$ is employed.

Figure 11 depicts the radar reflectivity cross-sections from a CPR and KaPR coincident event that occurred on 28 July 2016, over the Baltic Sea. The weather background at that time was that the atmospheric stratification was stable, the humidity in the lower atmosphere was high, and the vertical movement of the atmosphere was weak. The figure includes the original and combined reflectivity cross-sections and their average profiles.

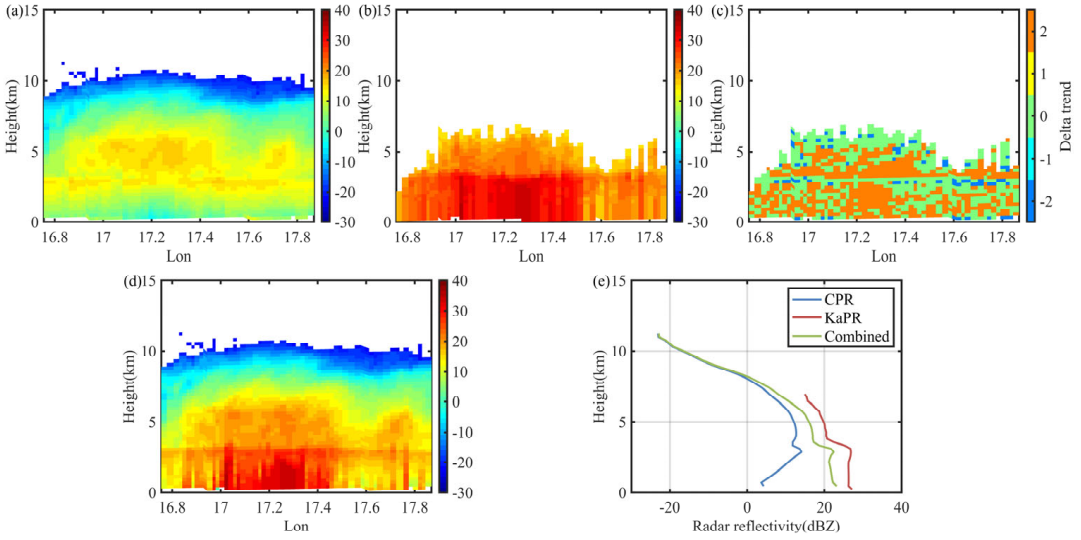

Figure 11. CPR and KaPR reflectivity and their synthesized cross-sections; average reflectivity of coincident case 1 ((**a**): CPR reflectivity cross-section, (**b**): KaPR reflectivity cross-section, (**c**): gradient difference in reflectivity of the two radars, (**d**): synthesis of two radar reflectivity cross-sections, (**e**): average profiles for CPR, KaPR, and synthesized reflectivity).

The observations from this precipitation case reveal a distinct bright band at an altitude of 3 km, indicating stratiform precipitation. The radar reflectivity values for CPR and KaPR are presented in Figure 11a,b, respectively. The precipitation cloud information detected by CPR is 48.86% more than that detected by KaPR. Both radars effectively measure precipitation in the 3–5 km altitude range. However, below 3 km, notable differences emerge in the reflectivity between the two radars. CPR experiences attenuation due to raindrop particles, hindering its ability to accurately indicate the location of strong echoes. Conversely, KaPR provides a clearer depiction of strong echoes below 3 km. The reflectivity gradient difference diagram in Figure 11c confirms that, below 3 km, the reflectivity of the two radars exhibits opposite trends as the altitude decreases. Figure 11d,e display the synthesized reflectivity and average profiles from both radars. Combining data from both radar frequencies allows for a comprehensive representation of the cloud/precipitation structure. The smaller ice particles at the top of the cloud system exhibit minimal attenuation of the W band, with the difference between the band conversion and the original reflectivity staying within 0.5 dB. As the moisture content increases below 5 km, the attenuation of the W band by precipitation particles gradually intensifies. Consequently, the weight of the KaPR reflectivity in the synthetic profile also increases gradually, bringing the synthesized reflectivity closer to the measured value in the Ka band.

Figure 12 illustrates the radar reflectivity cross-sections from a CPR and KaPR coincident event that took place on 13 June 2016, along the Gulf Coast of Louisiana, USA. The precipitation in this case extended up to 15 km in altitude, indicating a convective precipitation. The radar reflectivity values for CPR and KaPR are displayed in Figure 12a,b, respectively. CPR detected more precipitation cloud information than KaPR, accounting for 48.83%. Strong precipitation was observed in the area below 5 km, specifically between 93.5 and 93.6 degrees west. In this region, the CPR electromagnetic waves experience substantial interference and attenuation. Conversely, KaPR reflectivity provides a more accurate characterization in this region.

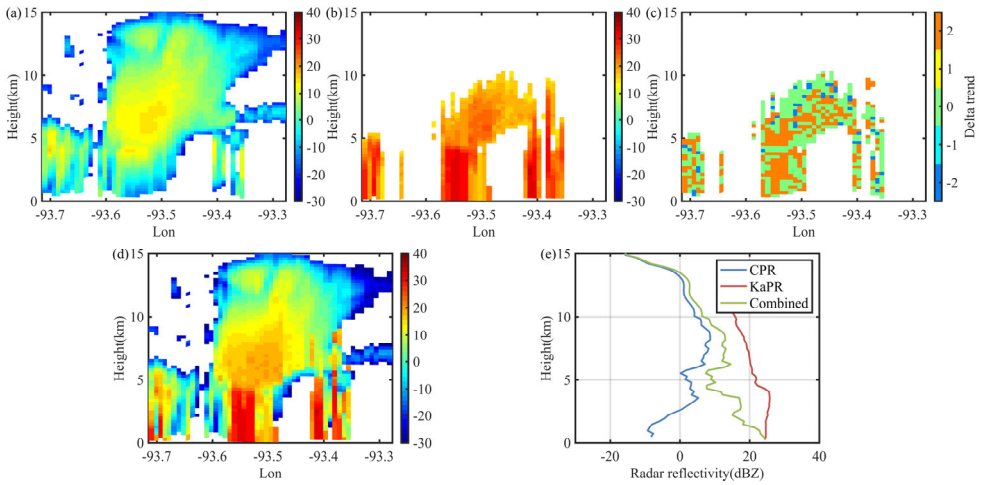

Figure 12. CPR and KaPR reflectivity cross-sections, and their synthesized cross-sections, for coincident case 2 ((**a**): CPR reflectivity, (**b**): KaPR reflectivity, (**c**): gradient difference in reflectivity of the two radars, (**d**): synthesized reflectivity cross-section, (**e**): average profiles for CPR, KaPR, and synthesized reflectivity).

A yellow area is evident in the W-band reflectivity near the 14 km altitude in Figure 12a. Above 10 km altitude, there may be a vigorous upward motion, causing the air within the precipitation system to rise rapidly to around 14 km and then cool rapidly. This process leads to the continuous condensation and growth of ice particles, resulting in larger ice crystals. These larger ice crystals generate strong radar wave reflections. A similar feature can also be observed near 14 km in the average radar reflectivity factor profile in Figure 12e, culminating in a peak.

Figure 12d shows the synthesized reflectivity from case 2, obtained by combining data from both radars. This synthesis yields a comprehensive representation of the cloud/precipitation structure, allowing for a more comprehensive assessment of the cloud characteristics associated with convective precipitation.

Data from the Level 2B GPM Combined Radar–Radiometer Precipitation Algorithm (2BCMB) were used to verify the synthesized results. The 2BCMB precipitation algorithm integrates Level 2 calibrated reflectivity profiles from the DPR and Level 1C GMI brightness temperatures. An a priori database of particle size distributions and corresponding environmental conditions was used to accurately retrieve precipitation data [32].

To demonstrate the performance of the synthesized reflectivity cross-section, we used the Spearman rank correlation coefficient between the 2BCMB precipitation rate and the radar reflectivity to analyze the performance of the synthesis. There is a relationship between the precipitation rate and radar reflectivity, because radar reflectivity is usually used to describe the intensity of scattering of radar waves by particles in the atmosphere (such as raindrops, snow, etc.). High radar reflectivity is generally associated with greater precipitation rates, and the Spearman rank correlation coefficient works for the monotonic relationship [33].

The Spearman rank correlation coefficient parameters (r_s) are defined as follows:

$$r_s = 1 - \frac{6\sum_{i=1}^{n} d_i^2}{n(n^2-1)}$$

where n is the number of bins with radar echo values, while d_i is the grade difference between the radar reflectivity and precipitation rate. The statistical quantitative comparison results are shown in Table 2.

Table 2. The statistical quantitative comparison results for case 1 and case 2.

		KaPR	Combined
Case 1	Ice phase	0.8035	0.8956
	Mixed phase	0.8153	0.8989
	Liquid phase	0.9231	0.9028
Case 2	Ice phase	0.6058	0.6750
	Mixed phase	0.5863	0.6453
	Liquid phase	0.4177	0.5110

From the comparison results of the stratiform and convective cases shown in Figure 13, we can see that the stratiform case has better consistency. The r_s for stratiform rain reached 0.8 for all three kinds of phase particles. Compared to stratiform precipitation, convective precipitation is usually generated under unstable atmospheric conditions. The r_s for convective rain reached only about 0.4~0.6 for the three kinds of phase particles. From the comparison of the r_s before and after synthesis, as shown in Table 2, whether in stratiform or convective precipitation, the results of the non-liquid-phase bin are better, and the r_s values of the ice phase and mixed phase are increased by 12% and 10%, respectively. The DPR data, combined with data from GMI, contribute to more accurate precipitation rate estimates. With the addition of the W band, the synthesized reflectivity in the non-liquid-phase bin has a better correlation with the more accurate precipitation rate retrieval in 2BCMB. The addition of W-band radar can play a positive role in the non-liquid-phase radar bin. The synthesis results are better in the ice-phase bin than in the mixed-phase bin. There are many types of precipitation particles in the mixed-phase bin, and the estimation of radar reflectivity is not accurate enough.

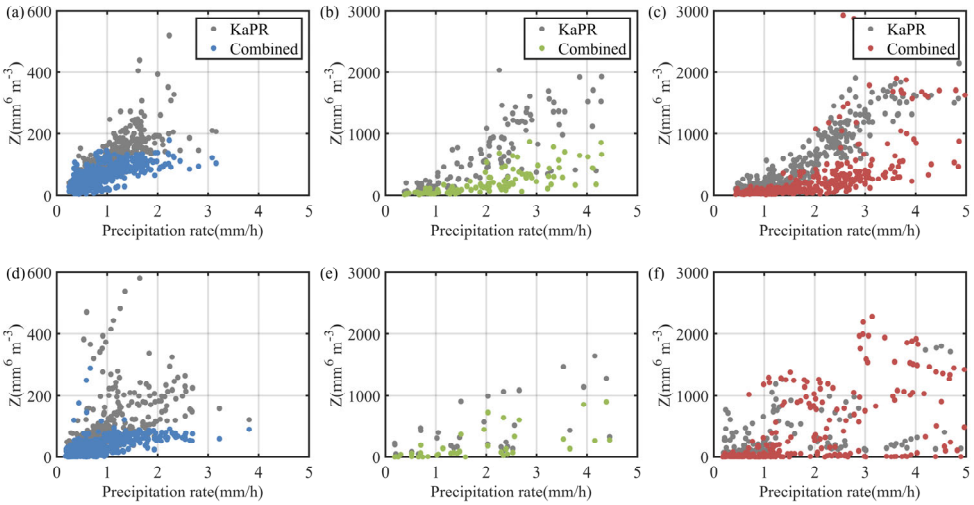

Figure 13. Scatterplots between the 2BCMB precipitation rate and KaPR reflectivity; synthesized reflectivity in different phases for cases 1 and 2 ((**a**): ice phase in case 1, (**b**): mixed phase in case 1, (**c**): liquid phase in case 1, (**d**): ice phase in case 2, (**e**): mixed phase in case 2, (**f**): liquid phase in case 2).

5. Discussion

This study compares and synthesizes the precipitation data from the coincidence of CPR and DPR observations, occurring within a ±15-min window, spanning from March 2014 to December 2017. The primary objective was to assess the disparities in radar reflectivity and precipitation rates between W- and Ka-band spaceborne radars, especially in diverse precipitation phases and varying intensities. Additionally, an attempt was made to synthesize the precipitation data from both radars to enhance the integrity and comprehensiveness of the precipitation information. The key findings of this investigation are as follows:

1. Radar reflectivity comparison: In convective rainfall, the presence of larger liquid particles leads to pronounced attenuation of W-band radar waves. Below the altitudes of the melting layer, CPR generally exhibits a decrease in reflectivity with decreasing altitude, while KaPR reflectivity tends to increase. In stratiform rainfall, where precipitation remains relatively stable, CPR reflectivity is predominantly found between 7 dBZ and 12 dBZ, whereas KaPR reflectivity is mainly distributed between 16 dBZ and 21 dBZ. Regarding snowfall, there is a peak around 10 km in the CPR snowfall average reflectivity profile, indicating that CPR can detect larger ice crystals formed during snowfall. Due to differences in radar sensitivity, the average echo-top height detected by CPR is approximately 3.6–4.2 km higher than that detected by KaPR, enabling CPR to capture more detailed vertical cloud structures.
2. Near-surface precipitation rate comparison: When comparing near-surface rain rates, the average near-surface rain rate of KaPR on the ocean surface is 0.4 mm/h higher than that of CPR within the range of 40 degrees north and south. This could be caused by the presence of large rainfall particles that lead to significant attenuation of CPR's electromagnetic waves, limiting its ability to accurately estimate rain rates beyond its upper threshold. However, at latitudes above 40 degrees, CPR's heightened sensitivity allows it to detect approximately 15% more near-surface rainfall events than KaPR, resulting in an average near-surface rain rate that is 0.1 mm/h greater than KaPR's. When comparing snowfall, it is important to note that for snowfall events influenced by terrain factors between 30 and 50 degrees north and south, CPR consistently retrieves lower values than KaPR. However, in areas with latitudes greater than 50 degrees, CPR detected more snowfall events than KaPR, accounting for 86% of the total snowfall events. In terms of near-surface snow rate comparisons, KaPR retrieves an average near-surface snow rate 0.2 mm/h higher than CPR's in regions below 50 degrees latitude. Conversely, in areas above 50 degrees latitude,

CPR's sensitivity leads to the detection of 45% more light snowfall events in the 0.01 mm/h class than KaPR, resulting in an average near-surface snowfall rate that is 0.1 mm/h higher than KaPR's.

3. Combining the near-surface precipitation rates of both radars allows for a more complete detection of precipitation, with rates ranging from 0.01 to 40 mm/h or higher levels. By synthesizing reflectivity from the CPR and KaPR, with consideration of their vertical gradient differences, a comprehensive cloud precipitation profile can be obtained. The precipitation cloud information detected by CPR but not KaPR accounted for 49% of the total cloud bodies on matching vertical sections. This reflectivity synthesis not only provides a complete view of the vertical structure of precipitation clouds, but also enables a more continuous reflectivity of precipitation cloud bodies. The Spearman rank correlation coefficient parameters for stratiform rain reached 0.8 for all three kinds of phase particles, while they only reached about 0.4~0.6 for the three kinds of phase particles for convective rain. This synthesis method works better in non-liquid-phase radar bins, whether in stratiform or convective precipitation, and the r_s of the ice phase and mixed phase are increased by about 12% and 10%, respectively, while the Spearman rank correlation coefficient of the precipitation rate and radar reflectivity is improved.

6. Conclusions

In this study, we compared the coincident data from CPR and KaPR from 2014 to 2017, and then a synthesis of the radar reflectivity from CPR and KaPR was attempted to obtain a complete cloud and precipitation structure. After comparing the near-surface precipitation rates, we found that the difference in near-surface precipitation rates between CPR and KaPR is related to the reflectivity gradient in the vertical direction. The greater the reflectivity gradient, the greater the difference in near-surface precipitation rates. Finally, the radar reflectivity was weighted and synthesized from CPR and KaPR based on the gradient difference of the reflectivity from the two radars. The results for a stratiform cloud and a deep convective case show that the synthesis can improve the consistency of reflectivity and precipitation rate measurements. In the future, the joint measurement of Ka and W bands holds the potential to establish a correlation between cloud properties and precipitation. This advancement is expected to deepen our comprehension of the cloud precipitation process, thereby contributing to an enhanced understanding of the intricacies involved in cloud-related precipitation phenomena. Additionally, the characteristics of the upper cloud system reflect the intensity and development trends of the lower-level rainfall system [34]. The combined use of the W and Ka bands offers a more objective and rational explanation of the connection between upper-level cloud structure and lower-level precipitation rates. Our next work will be to retrieve the precipitation rates of particles in different phases using combined W- and Ka-band radar data.

Author Contributions: Conceptualization, Y.L. and L.K.; methodology, Y.L, L.K. and Z.L.; software, H.G. and A.H.; validation, Y.L. and L.K.; formal analysis, L.K. and A.H.; investigation, Y.L.; resources, Y.X. and L.Z.; data curation, L.K. and Y.L.; writing—original draft preparation, Y.L.; writing—review and editing, L.K.; visualization, L.K.; supervision, L.K. and Y.X.; project administration, H.G.; funding acquisition, H.G. All authors have read and agreed to the published version of the manuscript.

Funding: This study was supported in part by the National Key Research and Development Program of China (2021YFC2802502), and in part by the Industry University Research Cooperation Fund of the Eighth Research Institute of China Aerospace Science and Technology Corporation and the National Natural Science Foundation of China (41975027).

Data Availability Statement: GPM data were downloaded from NASA PPS at https://storm.pps.eosdis.nasa.gov/storm/, accessed on 15 March 2022. CloudSat data were downloaded from the CloudSat data processing center at https://www.cloudsat.cira.colostate.edu/order/, accessed on 29 January 2022.

Acknowledgments: We acknowledge the data providers of the National Centers for the Environmental Prediction Final Operational Model Global Tropospheric Analyses. We would also like to thank the scientists and those who contributed to the CloudSat mission.

Conflicts of Interest: The authors declare no conflicts of interest.

References

1. Xie, P.; Arkin, P.A. Global Precipitation: A 17-Year Monthly Analysis Based on Gauge Observations, Satellite Estimates, and Numerical Model Outputs. *Bull. Am. Meteorol. Soc.* **1997**, *78*, 2539–2558. [CrossRef]
2. Bony, S.; Colman, R.; Kattsov, V.M.; Allan, R.P.; Bretherton, C.S.; Dufresne, J.-L.; Hall, A.; Hallegatte, S.; Holland, M.M.; Ingram, W.; et al. How Well Do We Understand and Evaluate Climate Change Feedback Processes? *J. Clim.* **2006**, *19*, 3445–3482. [CrossRef]
3. Kidd, C.; Kniveton, D.; Todd, M.C.; Bellerby, T. Satellite Rainfall Estimation Using Combined Passive Microwave and Infrared Algorithms. *J. Hydrometeorol.* **2003**, *4*, 1088–1104. [CrossRef]
4. Kidd, C.; Levizzani, V. Status of Satellite Precipitation Retrievals. *Hydrol. Earth Syst. Sci.* **2011**, *15*, 1109–1116. [CrossRef]
5. Kulie, M.S.; Milani, L.; Wood, N.B.; Tushaus, S.A.; Bennartz, R.; L'Ecuyer, T.S. A Shallow Cumuliform Snowfall Census Using Spaceborne Radar. *J. Hydrometeorol.* **2016**, *17*, 1261–1279. [CrossRef]
6. Hou, A.Y.; Kakar, R.K.; Neeck, S.; Azarbarzin, A.A.; Kummerow, C.D.; Kojima, M.; Oki, R.; Nakamura, K.; Iguchi, T. The Global Precipitation Measurement Mission. *Bull. Am. Meteorol. Soc.* **2014**, *95*, 701–722. [CrossRef]
7. Berg, W.; L'Ecuyer, T.; Haynes, J.M. The Distribution of Rainfall over Oceans from Spaceborne Radars. *J. Appl. Meteorol. Climatol.* **2010**, *49*, 535–543. [CrossRef]
8. Tang, G.; Wen, Y.; Gao, J.; Long, D.; Ma, Y.; Wan, W.; Hong, Y. Similarities and Differences between Three Coexisting Spaceborne Radars in Global Rainfall and Snowfall Estimation. *Water Resour. Res.* **2017**, *53*, 3835–3853. [CrossRef]
9. Sindhu, K.D.; Bhat, G.S. Comparison of CloudSat and TRMM Radar Reflectivities. *J. Earth Syst. Sci.* **2013**, *122*, 947–956. [CrossRef]
10. Fall, V.M.; Cao, Q.; Hong, Y. Intercomparison of Vertical Structure of Storms Revealed by Ground-Based (NMQ) and Spaceborne Radars (CloudSat-CPR and TRMM-PR). *Sci. World J.* **2013**, *2013*, 270726. [CrossRef]
11. Casella, D.; Panegrossi, G.; Sanò, P.; Marra, A.C.; Dietrich, S.; Johnson, B.E.; Kulie, M.S. Evaluation of the GPM-DPR Snowfall Detection Capability: Comparison with CloudSat-CPR. *Atmos. Res.* **2017**, *197*, 64–75. [CrossRef]
12. Mroz, K.; Montopoli, M.; Battaglia, A.; Panegrossi, G.; Kirstetter, P.-E.; Baldini, L. Cross-Validation of Active and Passive Microwave Snowfall Products over the Continental United States. *J. Hydrometeorol.* **2021**, *22*, 1297–1315. [CrossRef]
13. Skofronick-Jackson, G.; Kulie, M.; Milani, L.; Munchak, S.J.; Wood, N.B.; Levizzani, V. Satellite Estimation of Falling Snow: A Global Precipitation Measurement (GPM) Core Observatory Perspective. *J. Appl. Meteorol. Climatol.* **2019**, *58*, 1429–1448. [CrossRef]
14. Durden, S.L.; Tanelli, S.; Epp, L.W.; Jamnejad, V.; Long, E.M.; Perez, R.M.; Prata, A. System Design and Subsystem Technology for a Future Spaceborne Cloud Radar. *IEEE Geosci. Remote Sens. Lett.* **2016**, *13*, 560–564. [CrossRef]
15. Tanelli, S.; Haddad, Z.S.; Im, E.; Durden, S.L.; Sy, O.O.; Peral, E.; Sadowy, G.; Sanchez-Barbetty, M. Radar Concepts for the next Generation of Spacebome Observations of Cloud and Precipitation Processes. In Proceedings of the 2018 IEEE Radar Conference (RadarConf18), Oklahoma City, OK, USA, 23–27 April 2018; IEEE: Piscataway, NJ, USA, 2018. [CrossRef]
16. Wu, Q.; Yang, M.; Dou, F.; Guo, Y.; An, D. A Study of Cloud Parameters Retrieval Algorithm for Spaceborne Millimeter Wavelength Cloud Radar. *Acta Meteorol. Sin.* **2018**, *76*, 160–168. (In Chinese) [CrossRef]
17. Stephens, G.L.; Vane, D.G.; Tanelli, S.; Im, E.; Durden, S.; Rokey, M.; Reinke, D.; Partain, P.; Mace, G.G.; Austin, R.; et al. CloudSat Mission: Performance and Early Science after the First Year of Operation. *J. Geophys. Res.* **2008**, *113*, D00A18. [CrossRef]
18. Tanelli, S.; Durden, S.L.; Im, E.; Pak, K.S.; Reinke, D.G.; Partain, P.; Haynes, J.M.; Marchand, R.T. CloudSat's Cloud Profiling Radar After Two Years in Orbit: Performance, Calibration, and Processing. *IEEE Trans. Geosci. Remote Sens.* **2008**, *46*, 3560–3573. [CrossRef]
19. Bacmeister, J.T.; Stephens, G.L. Spatial Statistics of Likely Convective Clouds in CloudSat Data. *J. Geophys. Res.* **2011**, *116*, D04104. [CrossRef]
20. Riley, E.M.; Mapes, B.E. Unexpected Peak near −15 °C in CloudSat Echo Top Climatology. *Geophys. Res. Lett.* **2009**, *36*, L09819. [CrossRef]
21. Marchand, R.; Mace, G.G.; Ackerman, T.; Stephens, G. Hydrometeor Detection Using Cloudsat—An Earth-Orbiting 94-GHz Cloud Radar. *J. Atmos. Ocean. Technol.* **2008**, *25*, 519–533. [CrossRef]
22. Behrangi, A.; Christensen, M.; Richardson, M.; Lebsock, M.; Stephens, G.; Huffman, G.J.; Bolvin, D.; Adler, R.F.; Gardner, A.; Lambrigtsen, B.; et al. Status of High-Latitude Precipitation Estimates from Observations and Reanalyses. *J. Geophys. Res. Atmos.* **2016**, *121*, 4468–4486. [CrossRef]
23. Wood, N.B.; L'Ecuyer, T.S.; Heymsfield, A.J.; Stephens, G.L.; Hudak, D.R.; Rodriguez, P. Estimating Snow Microphysical Properties Using Collocated Multisensor Observations. *J. Geophys. Res. Atmos.* **2014**, *119*, 8941–8961. [CrossRef]
24. Rodgers, C.D. Retrieval of Atmospheric Temperature and Composition from Remote Measurements of Thermal Radiation. *Rev. Geophys.* **1976**, *14*, 609. [CrossRef]

25. Hamada, A.; Takayabu, Y.N. Improvements in Detection of Light Precipitation with the Global Precipitation Measurement Dual-Frequency Precipitation Radar (GPM DPR). *J. Atmos. Ocean. Technol.* **2016**, *33*, 653–667. [CrossRef]
26. Iguchi, T.; Seto, S.; Meneghini, R.; Yoshida, N.; Awaka, J.; Kubota, T. *GPM/DPR Level-2 Algorithm Theoretical Basis Document*; NASA Goddard Space Flight Center: Washington, DC, USA, 2023.
27. Joseph Turk, F.; Ringerud, S.; Camplani, A.; Casella, D.; Chase, R.J.; Ebtehaj, A.M.; Gong, J.; Kulie, M.S.; Liu, G.; Milani, L.; et al. Applications of a CloudSat-TRMM and CloudSat-GPM Satellite Coincidence Dataset. *Remote Sens.* **2021**, *13*, 2264. [CrossRef]
28. Yin, M.; Liu, G.; Honeyager, R.; Joseph Turk, F. Observed Differences of Triple-Frequency Radar Signatures between Snowflakes in Stratiform and Convective Clouds. *J. Quant. Spectrosc. Radiat. Transf.* **2017**, *193*, 13–20. [CrossRef]
29. Dong, C. Remote Sensing, Hydrological Modeling and in Situ Observations in Snow Cover Research: A Review. *J. Hydrol.* **2018**, *561*, 573–583. [CrossRef]
30. Chen, S.; Hong, Y.; Kulie, M.S.; Behrangi, A.; Stepanian, P.M.; Cao, Q.; You, Y.; Zhang, J.; Hu, J.; Zhang, X. Comparison of Snowfall Estimates from the NASA CloudSat Cloud Profiling Radar and NOAA/NSSL Multi-Radar Multi-Sensor System. *J. Hydrol.* **2016**, *541*, 862–872. [CrossRef]
31. Kou, L.; Lin, Z.; Gao, H.; Liao, S.; Ding, P. Simulation and Sensitivity Analysis for Cloud and Precipitation Measurements via Spaceborne Millimeter-Wave Radar. *Atmos. Meas. Tech.* **2023**, *16*, 1723–1744. [CrossRef]
32. Olson, W. *GPM Combined Radar-Radiometer Precipitation Algorithm Theoretical Basis Document (Version 5)*; NASA: Washington, DC, USA, 2018.
33. Rosenblad, A. The Concise Encyclopedia of Statistics. *J. Appl. Stat.* **2011**, *38*, 502. [CrossRef]
34. Tang, L.; Gao, W.; Xue, L.; Zhang, G.; Guo, J. Climatological Characteristics of Hydrometeors in Precipitating Clouds over Eastern China and Their Relationship with Precipitation Based on ERA5 Reanalysis. *J. Appl. Meteorol. Climatol.* **2023**, *62*, 625–641. [CrossRef]